A novel skutterudite phase in the Ni–Sb–Sn system: phase equilibria and physical properties

A novel skutterudite phase in the Ni–Sb–Sn system: phase equilibria and physical properties

A Grytsiv[1], P Rogl[1,10], St Berger[2], Ch Paul[2], H Michor[2], E Bauer[2], G Hilscher[2], C Godart[3,4], P Knoll[5], M Musso[6], W Lottermoser[7], A Saccone[8], R Ferro[9], T Roisnel[9] and H Noel[9]

[1] Institut für Physikalische Chemie, Univ. Wien, Währingerstr. 42, A-1090 Wien, Austria
[2] Institut für Festkörperphysik, TU Wien, A-1040 Wien, Wiedner Hauptstr. 8–10, Austria
[3] CNRS-UPR209, ISCSA, 2-8 rue Henri Dunant, F94320 Thiais, France
[4] LURE, CNRS, Universite Paris Sud, 91405 Orsay, France
[5] Institut für Experimentalphysik, Universität Graz, Universitätsplatz 5, A-8010 Graz, Austria
[6] Institut für Physik und Biophysik, Universität Salzburg, Hellbrunnerstr. 34, A-50120 Salzburg, Austria
[7] Institut für Mineralogie, Universität Salzburg, Hellbrunnerstr. 34, A-50120 Salzburg, Austria
[8] Dipartimento di Chimica e Chimica Industriale, Universita di Genova, I-16146 Genova, Italy
[9] Laboratoire de Chimie du Solide et Inorganique Moléculaire, Université de Rennes I, UMR CNRS-6511, Avenue du Général Leclerc, F-35042 Rennes Cedex, France

E-mail: peter.franz.rogl@univie.ac.at

Abstract

A novel ternary phase, $Sn_yNi_4Sb_{12-x}Sn_x$, has been characterized and found to exhibit a wide range of homogeneity (at 250 °C, $2.4 \leqslant x \leqslant 5.6$, $0 \leqslant y \leqslant 0.31$; at 350 °C, $2.7 \leqslant x \leqslant 5.0$, $0 \leqslant y \leqslant 0.27$). $Sn_yNi_4Sb_{12-x}Sn_x$ crystallizes in a skutterudite-based structure in which Sn atoms are found to occupy two crystallographically inequivalent sites: (a) Sn and Sb atoms randomly share the 24g site; and (b) a small fraction of Sn atoms occupy the 2a $(0, 0, 0)$ position, with an anomalously large isotropic atomic displacement parameter. $Eu_{0.8}Ni_4Sb_{5.8}Sn_{6.2}$, $Yb_{0.6}Ni_4Sb_{6.7}Sn_{5.3}$ and $Ni_4As_{9.1}Ge_{2.9}$ are isotypic skutterudites. Depending on the particular composition, metallic as well as semiconducting states appear. The crossover from semiconducting to metallic behaviour is discussed in terms of a temperature-dependent carrier concentration employing a simple model density of states with the Fermi energy slightly below a narrow energy gap. This model accounts for the peculiar temperature-dependent electrical resistivity. These skutterudites are characterized by a number of lattice vibrations, which were elucidated by Raman measurements and compared to the specific heat data. The Eu-containing compound exhibits long-range magnetic order at $T_{mag} \approx 6$ K, arising from the Eu^{2+} ground state.

[10] Author to whom any correspondence should be addressed.

1. Introduction

Skutterudite-based materials reveal a large variety of physical properties, among them attractively high Seebeck coefficients in combination with low thermal conductivity: a prerequisite for high-performance thermoelectric devices. Skutterudites crystallize in the structure type of $CoAs_3$ (space group $Im\bar{3}$) of which the $LaFe_4P_{12}$ structure is a filled variant. The chemical formula of these compounds can be described as $E_yT_4X_{12}$, where T is a transition element of the VIII group in the 8c position (1/4, 1/4, 1/4); E occupies the icosahedral hole position 2a (0, 0, 0) which can be filled by a number of electropositive elements such as Ca, Sr, Tl, lanthanides and actinides, or under special conditions by Y, Hf [1, 2] Pb and Sn [3–6] (high-pressure or multilayer precursor methods) and Na in nanowire state [7]; X is a pnictogen or one of the IVA–VIA elements at the 24g site (0, y, z). It is interesting to note that Sn atoms were found to be able to occupy the 24g site ($Co_4Sb_{12-y}Sn_y$ [8], $CoSn_6Te_6$ [9], $La_{1-x}Co_4Sb_{12-y}Sn_y$ [10], $Yb_{1-x}Co_4Sb_{12-y}Sn_y$ [11], $Tl_{1-x}Co_4Sb_{12-y}Sn_y$ [12]) as well as the 2a site ($Sn_{1-x}Fe_4Sb_{12}$ [13], $Sn_{1-x}Co_4Sb_{12}$ [3–6]): Sn-filled skutterudites are generally characterized by an anomalously large isotropic atomic displacement parameter for tin in the 2a position.

Although NiP_3 is reported to exist [14, 15], the homologous skutterudites $NiAs_3$ and $NiSb_3$ do not form [16, 17] and there are no data on the existence of ternary nickel-based skutterudites, $E_yNi_4X_{12}$, where only nickel atoms occupy the 8c position. There are, however, data on a mixed compound $Fe_2Ni_2Sb_{12}$ [18] and solid solutions of it with some other skutterudites such as $CeFe_4Sb_{12}$ [19–21], $YbFe_4Sb_{12}$ [22] and $EuFe_4Sb_{12}$ [23]. In order to remedy the lack of information on the nickel-based systems Ni–Sb–X and because of the interesting properties reported in the literature for tin-containing skutterudites, we performed a systematic investigation of the Ni–Sb–Sn ternary system. There are limited data on phase equilibria in this system, which only concern the Ni–NiSb–Ni_3Sn_2 composition range [24–28]. Phase relations in the remaining part of this system: Sb–Sn–Ni_3Sn_2–NiSb are unknown and therefore this region was chosen as the topic of interest here, with extension to related systems: Ni–Co–Sb–Sn, Ni–As–Ge and (Ce, Pr, Eu, Yb)–Ni–Sb–Sn. In this paper we are going to show that:

 (i) germanium and tin are able to stabilize the hypothetical binary skutterudite phases $NiAs_3(Ni_4As_{9.1}Ge_{2.9})$ and $NiSb_3(Sn_yNi_4Sb_{12-x}Sn_x)$;
 (ii) $Sn_yNi_4Sb_{12-x}Sn_x$ has a wide homogeneity region and shows a continuous increase of y with increasing x;
(iii) large isotropic displacement parameters exist for the Sn atom at the 2a site.

Moreover, we evaluate physical properties to characterize this new class of skutterudites and probe their thermoelectric performance.

2. Experimental details

Bulk alloys, each with a total weight of 1.5–3 g, were synthesized by argon arc melting of compacted tablets of elemental powders (Ni, Sb, Sn) and Eu/Yb pieces of 99.9 mass% minimum purity on a water-cooled copper hearth. Total weight losses of 1–3 mass% were attributed to evaporation of antimony and/or Eu/Yb and were compensated. The alloys were vacuum sealed in quartz ampoules and annealed at 350, 300 and 250 °C for 4–30 days prior to quenching in cold water. Tin-rich single crystals of $Sn_yNi_4Sb_{12-x}Sn_x$ were prepared from Sn flux starting from a composition 3Ni–14Sb–83Sn (at.%) by soaking at 700 °C for 12 h, then cooling at a rate of 10 °C h^{-1} to 300 °C; they were then kept at this temperature for 72 h to reach equilibrium. Subsequently the sample was removed from the furnace and treated in 37%

Table 1. Crystal structure data for unary and binary phases in the system Ni–Sb–Sn.

Phase	Pearson symbol	Space group	Structure type	Lattice parameters a (nm)	b (nm)	c (nm)	β (deg)	Reference
(Sb)	$hR2$	$R\bar{3}m$	As	0.430 07	—	1.122 2	—	[17]
(Sn)	$tI2$	$I4/mmm$	In	0.583 13	—	0.318 15	—	[17]
NiSb	$hP4$	$P6_3/mmc$	NiAs	0.393 25	—	0.513 51	—	[17]
NiSb$_2$	$oP6$	$Pnnm$	FeS$_2$	0.518 25	0.631 68	0.384 30	—	[17]
HT-Ni$_3$Sn$_2$	$hP6$	$P6_3/mmc$	Ni$_2$In	0.414 6	—	0.525 3	—	[17]
LT-Ni$_3$Sn$_2$	$oP20$	$Pnma$	Ni$_3$Sn$_2$	0.706 15	0.515 30	0.809 03	—	[17]
Ni$_3$Sn$_4$	$mC16$	$C2/m$	CoGe	1.211 99	0.406 09	0.522 38	105.17	[17]
SbSn	$hR2$	Rhombohedral	Distorted, NaCl	0.432 6	—	1.063 9	—	[40]
Sb$_2$Sn$_3$	$cF8$	$Fm\bar{3}m$	NaCl	0.615	—	—	—	[38]

HCl hot acid to dissolve the Sn-rich matrix. Ni$_4$As$_9$Ge$_3$ was prepared from elemental powder compacts, which were slowly heated to 800 °C in an evacuated quartz tube and kept at this temperature in liquid state for 12 h. The powdered specimen was recompacted and annealed at 600 °C for eight days. After this procedure it was found to be a single-phase skutterudite.

The characterization, comprising light optical microscopy (LOM), wavelength-dispersive electron microprobe analyses (EMPA), Guinier–Huber x-ray image plate or D5000 powder diffractometer readings for quantitative Rietveld refinement employing the FULLPROF program [29], can be found from [30]. Weissenberg photographs accomplished crystal quality control and allowed inspection of the crystal symmetry. Single-crystal x-ray intensity data were collected on a Nonius Kappa CCD four-circle diffractometer; data and structure refinement were performed with the programs DENZO, SORTAV [31], SHELXS-97 [32]. Bulk properties (temperature-dependent resistivity, temperature-dependent thermal conductivity and thermopower as well as x-ray absorption spectroscopy, magnetic susceptibility and specific heat) were obtained by a variety of standard techniques, described in detail in [33].

Two samples, Ni$_4$Sb$_9$Sn$_3$ and Sn$_{0.21}$Ni$_4$Sb$_{7.1}$Sn$_{4.9}$, were prepared as Mössbauer absorbers (5 mg Sn cm^{-2}, 7 mm diameter). A conventional Mössbauer apparatus was used with a 10 mCi source (initial activity) of ^{119}Sn^m in a CaSnO$_3$ matrix. Measurements were made on a SnO$_2$ absorber in order to determine the calibration factor. A comprehensive description of the experimental technique is given in [34]. Lattice vibrations have been monitored by Raman spectroscopy. Measurements were made on small (about 500 μm $\times$ 500 μm $\times$ 20 μm) single crystals of Sn$_{0.3}$Ni$_4$Sb$_{6.4}$Sn$_{5.6}$ with all available polarization directions of the incident laser beam (514.5 nm) and the scattered radiation at room temperature using the scanning multichannel technique [35].

3. Results and discussion

3.1. Phase equilibria

The binary phase diagrams for Ni–Sb and Ni–Sn were described by [16]. Phase equilibria in the Sb–Sn system after [36] were confirmed as most reliable in a number of recent investigations concerning also a thermodynamic assessment of this system [37–40]. Homogeneity regions of solid phases were accepted after thermodynamic assessments of [37, 40]. Crystal structure data on the relevant solid phases are presented in table 1.

Compositions of the alloys investigated (figures 1 and 2) lie within the partial system formed by pure antimony and tin, on one side, and by the two congruent melting compounds,
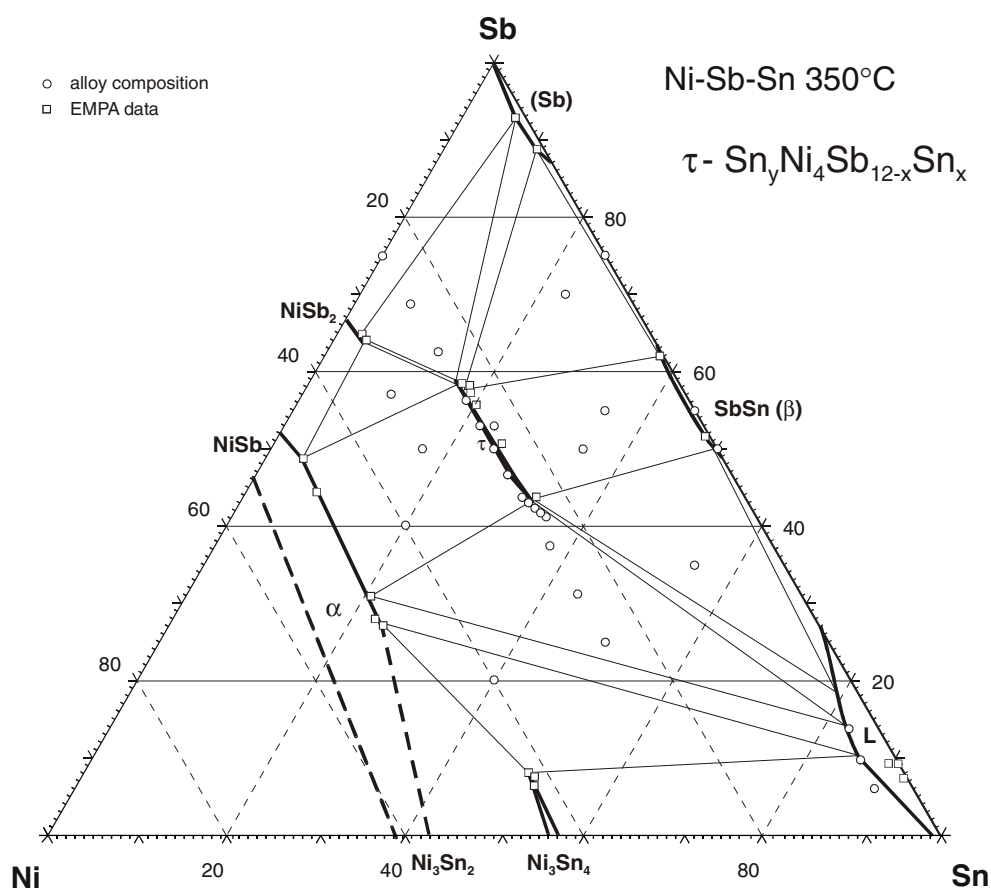
Figure 1. The isothermal section of the Ni–Sb–Sn ternary system at 350 °C.

Ni$_3$Sn$_2$ and NiSb, on the other. The latter two compounds have related crystal structures (table 1) and form a continuous solid solution [26, 28], which separates the Ni–Sb–Sn ternary system into two independent subsystems. As a consequence, phase equilibria in these two subsystems can be investigated independently.

X-ray analyses of as-cast samples show that the major phase crystallizing in the Sb–Sn–NiSb–Ni$_3$Sn$_2$ system is the NiSb–Ni$_3$Sn$_2$ solid solution (α), which has a wide primary crystallization field extending deeply into the ternary system, thereby reaching compositions near the Sb–Sn binary. This phase was found in all as-cast samples and in equilibrium with all other phases, a fact explained by its high thermodynamic stability. The same situation was observed for samples annealed at 600 and 500 °C, where the solid solution α also plays a dominant role in the determination of phase equilibria. A different situation was met in samples annealed at 400 and 450 °C, where x-ray patterns reveal the presence of a novel ternary phase, usually found in a non-equilibrium four-phase mixture with binary phases. In view of the low melting temperatures of Sb–Sn binary alloys, ternary samples were annealed at temperatures of 350 and 250 °C. The results obtained from x-ray and microprobe analyses are summarized in two isothermal sections (figures 1 and 2) and in table 2. The novel ternary phase Sn$_y$Ni$_4$Sb$_{12-x}$Sn$_x$ (τ) was found to exist in most of the annealed ternary alloys and, after
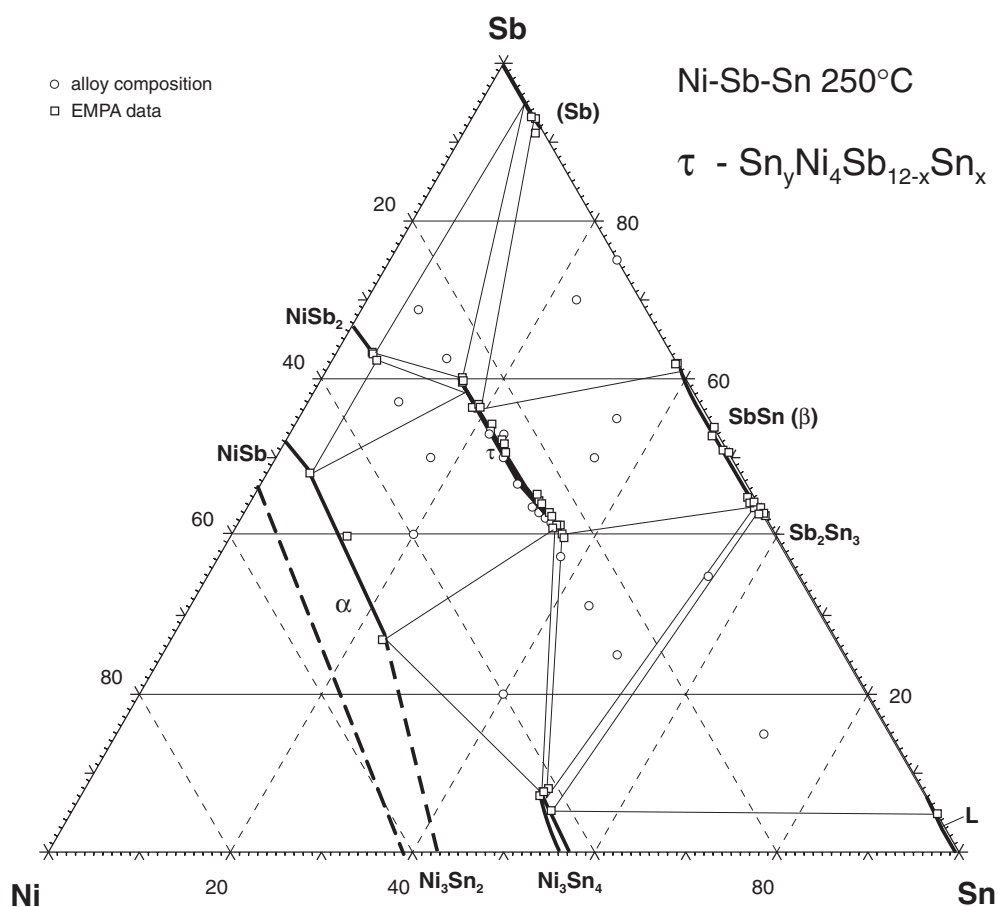
Figure 2. The isothermal section of the Ni–Sb–Sn ternary system at 250 °C.

preliminary inspection by means of powder x-ray diffraction, a crystal structure related to the $CoAs_3$ type was assigned. Lattice parameters of this phase vary strongly from sample to sample, indicating a large homogeneity region of this phase, confirmed by microprobe measurements and by the variation of lattice parameters versus the atomic ratio $Sn/(Sb + Sn)$ (see figure 3(a)). The homogeneity region extends at 350 °C for atomic ratios $0.215 < Sn/(Sn + Sb) < 0.432$ and expands at 250 °C up to a value of 0.475. Although the skutterudite-based phase was only found in samples annealed at low temperature, it certainly forms from liquid phase as seen from the microstructure of annealed samples (figure 4), where the skutterudite phase was found in the shape of dendrites, a kind of crystallization, only explained by formation from a liquid. This fact enabled us to grow tin-rich skutterudite single crystals from the tin-rich liquid.

After annealing at 350 °C the tin-rich alloys were found to be in a non-equilibrium condition containing four phases. Samples with the skutterudite phase were found in non-equilibrium with α, β and tin-based solid solutions, whilst the alloys 40Ni–20Sb–40Sn (at.%) contained the three latter phases and Ni_3Sn_4. EMPA of the Sn-based phase in these samples yielded a composition 1Ni–9.3Sb–89.7Sn close to that reported as the maximal binary solubility of Sb in (Sn). After additional annealing at 250 °C the tin-rich samples were found to be in equilibrium, shown in the phase diagram in figure 2. There is neither equilibrium of the
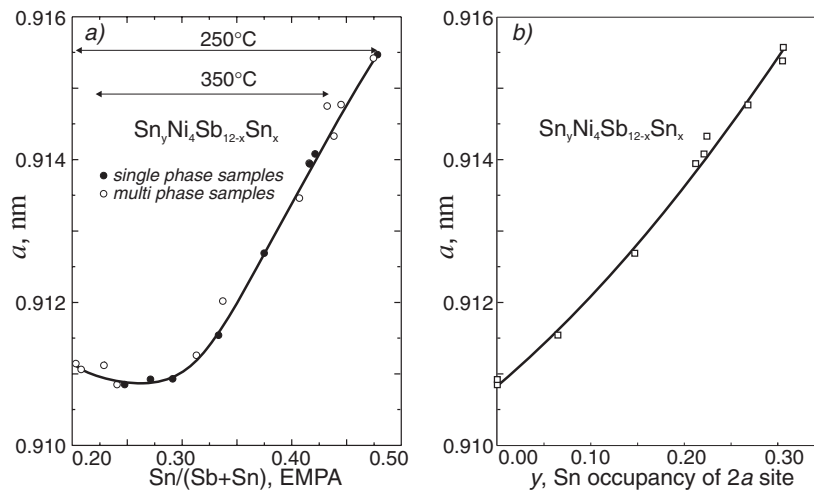
Figure 3. Lattice parameter of $Sn_yNi_4Sb_{12-x}Sn_x$ as a function of $Sn/(Sn + Sb)$ atomic ratio (a), and occupancy of the 2a site by Sn (b).
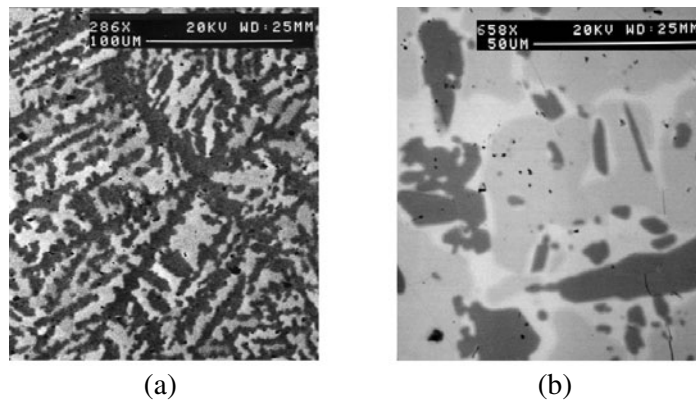
Figure 4. The microstructure of Ni–Sb–Sn alloys: (a) 15Ni–50Sb–35Sn (at.%) annealed at 350 °C for 14 days: skutterudite—black phase, β—white phase; (b) 25Ni–31Sb–44Sn (at.%) annealed at 250 °C for 20 days: skutterudite—grey phase, α—black phase, β—white phase.

skutterudite phase nor equilibrium of the α-phase with the tin-based solid solution. On the basis of these data as well as from the sample location and compositions of the solid phases determined by EMPA, phase equilibria were established in the tin corner of the phase diagram at 350 °C. The region of the liquid in equilibrium with the skutterudite phase was estimated from the observations made when growing single crystals from the tin-rich liquid. Thus, the sample 3Ni–14Sb–83Sn (at.%) was held in the liquid state at 350 °C for one week, and subsequent dissolution of the tin matrix in HCl resulted in a product which, from x-ray analysis, consists mainly of α and only contains a small amount of skutterudite. The skutterudite was found in the form of small thin crystals, with the α-phase in ill-shaped dendrites. Completely different results were obtained after treatment of this sample at 300 °C. The product then contained well-shaped crystals of β-phase and conglomerates of skutterudite crystals. From this we may conclude that the alloy 3Ni–14Sb–83Sn (at.%) at 350 °C was completely in the liquid state and

Table 2. Three-phase equilibria, lattice parameters and phase composition of the Ni–Sb–Sn system.

Phase region[a] T (°C)	Phase	Composition (EMPA; at.%)			Lattice parameters			
		Ni	Sb	Sn	a (nm)	b (nm)	c (nm)	β (deg)
(Sb) + NiSb$_2$ + τ	(Sb)	1.2	92.7	6.1	0.427 34(5)	—	1.143 2(9)	—
350	NiSb$_2$	32.3	64.7	3.0	0.517 96(7)	0.633 2(2)	0.382 71(7)	—
	τ	24.5	60.2	15.3	0.911 20(1)	—	—	—
NiSb$_2$ + α + τ	NiSb$_2$	32.3	69.3	3.8	0.518 07(4)	0.633 58(7)	0.382 39(3)	—
350	α	47.0	48.6	4.4	0.392 44(1)	—	0.513 72(6)	—
	τ	24.4	58.3	17.3	0.911 12(2)	—	—	—
(Sb) + β + τ	(Sb)	0.8	88.7	10.5	0.425 75(6)	—	1.145 9(2)	—
350	β	0.4	61.9	37.7	0.432 31(4)	—	1.076 0(1)	—
	τ	23.6	58.0	18.4	0.910 85(4)	—	—	—
L + β + τ	L(Sn)[b]	2	19	79	0.584 27(5)	—	0.318 15(2)	
350	β[b]	—	50	50	0.432 42(6)	—	1.066 8(6)	—
	τ[b]	24	44	32	0.913 66(2)	—	—	—
L + α + τ	L(Sn)[b]	3	14	83	0.584 34(4)		0.318 15(3)	—
350	α	48.3	30.8	20.9	0.393 60(2)	—	0.510 45(8)	—
	τ	23.3	43.7	33.0	0.914 75(2)	—	—	—
L + α + Ni$_3$Sn$_4$	L(Sn)[b]	3	10	87	0.584 20(0)	—	0.318 16(0)	—
350	α	49.4	28.0	22.6	0.393 75(0)	—	0.509 92(1)	—
	Ni$_3$Sn$_4$	42.4	6.5	51.1	1.219 1(6)	0.405 93(0)	0.522 25(6)	104.87(1)
(Sb) + NiSb$_2$ + τ	(Sb)	1.0	91.1	7.8	0.426 95(1)	—	1.141 34(2)	—
250	NiSb$_2$	32.8	63.2	4.0	0.517 96(1)	0.633 13(2)	0.382 54(2)	—
	τ	24.6	59.8	15.6	0.911 09(1)	—	—	—
NiSb$_2$ + α + τ	NiSb$_2$	32.8	62.4	4.8	0.518 03(1)	0.633 74(2)	0.382 12(1)	—
250	α	47.3	48.1	4.6	0.392 17(1)	—	0.513 35(2)	—
	τ	25.3	56.4	18.3	0.910 45(1)	—	—	—
(Sb) + β + τ	(Sb)	—	87.9	12.1	0.426 63(5)	—	1.144 8(3)	—
250	β	—	62.0	38.0	0.432 78(9)	—	1.073 2(1)	—
	τ	24.4	56.8	18.8	0.910 98(2)	—	—	—
α + Ni$_3$Sn$_4$ + τ	α	49.6	26.8	23.0	0.394 42(1)	—	0.509 77(2)	
250	Ni$_3$Sn$_4$	41.5	7.3	51.2	1.218 8(2)	0.406 15(1)	0.522 51(7)	104.89(1)
	τ	24.2	41.0	34.8	0.914 50(2)			
β + Ni$_3$Sn$_4$ + τ	β	0.6	43.6	55.8	0.432 81(3)	—	1.066 3(3)	—
250	Ni$_3$Sn$_4$	41.8	7.6	50.6	1.218 5(3)	0.406 08(4)	0.522 31(9)	104.91(1)
	τ	23.4	40.6	36.4	0.915 42(2)	—	—	—
L + β + Ni$_3$Sn$_4$	L(Sn)	~0	4.9	95.1	0.584 20(1)	—	0.318 28(1)	—
250	β	~0	42.7	57.3	0.432 21(1)	—	1.068 41(2)	—
	Ni$_3$Sn$_4$	42.2	5.3	52.5	1.218 8(2)	0.405 99(1)	0.522 22(2)	104.92(1)

[a] The symbols used are: α for the continuous solid solution of NiSb–Ni$_3$Sn$_2$, β for SbSn and τ for Sn$_y$Ni$_4$Sb$_{12-x}$Sn$_x$.
[b] The composition of this phase was estimated.

that the sample composition lies close to the tie line, liquid + α phase, which appears on slight decrease of the temperature. On lowering the temperature by 50 °C, the phase equilibria change dramatically: equilibrium of skutterudite with β-phase and tin-rich liquid arises. Comparing this result with the two isothermal sections, we expect a strong change in phase equilibria on lowering the temperature from 350 to 250 °C, suggesting at least two invariant equilibria in this temperature range. The reaction scheme becomes more complicated if one takes into

account the Sb_2Sn_3 phase, which was not observed in this investigation, because in the binary system it exists only in a small temperature range of 324–242 °C and it is difficult to quench. For consistency with the accepted binary Sb–Sn system, the Sb_2Sn_3 phase was introduced in the isothermal section at 250 °C.

Interesting behaviour was detected for the continuous solid solution of the α-phase formed by the binary compounds NiSb and Ni_3Sn_2, which have closely related crystal structures differing only by one additional crystallographic position for Ni atoms in Ni_3Sn_2 (Ni_2In) with respect to the NiSb (NiAs) counter-phase. A smooth increase of lattice parameters within the NiSb–Ni_3Sn_2 solid solution from $a = 0.3936$ nm and $c = 0.5137$ nm (NiSb) to $a = 0.4110$ nm and $c = 0.5182$ nm (Ni_3Sn_2) was reported by [24]. In spite of such behaviour, the lattice parameters of the α-phase in ternary alloys show values very close to those obtained for the NiSb phase in the nickel-poor side of the binary system: $a = 0.39091(2)$ nm and $c = 0.51311(3)$ nm. A simple explanation can be found in Sb/Sn substitution in the NiSb lattice (NiAs structure type) on the Ni-poor side of this solid solution. EMPA confirmed the fact that the nickel content of the nickel-poor solid solution α is practically constant for a wide range of Sn/Sb ratios, where this phase coexists in equilibrium with the skutterudite (figures 1 and 2).

3.2. Crystal structure and Mössbauer spectra

Rietveld refinements of the x-ray powder spectra of the new materials, $Sn_yNi_4Sb_{12-x}Sn_x$, $Eu_{0.8}Ni_4Sb_{5.8}Sn_{6.2}$, $Yb_{0.6}Ni_4Sb_{6.7}Sn_{5.3}$, $Ni_4As_{9.1}Ge_{2.9}$ were all consistent with the skutterudite structure (of $LaFe_4Sb_{12}$ or $CoAs_3$ type). The refinements, in combination with EMP analyses, were used to determine the degree of filling of the void in the 2a position but also to monitor the Sb/Sn and As/Ge concentration (see table 3). For the arsenide, EMPA data revealed a formula of $Ni_4As_{9.1}Ge_{2.9}$. As $Yb_{0.6}Ni_4Sb_{6.7}Sn_{5.3}$ ($a = 0.91399(1)$ nm) contained minor amounts of the Sn-filled skutterudite phase, we did not perform quantitative refinement.

From the concentration-dependent lattice parameters of the skutterudite phase $Sn_yNi_4Sb_{12-x}Sn_x$, presented in figure 3(a), we can see a rather interesting behaviour, which cannot be explained by simple random substitution of Sn for Sb atoms in the 24g site. While the insignificant change of the lattice parameters at small tin atom ratios Sn/(Sn + Sb) from 0.2 to 0.275 arises from simple substitution of tin for antimony in the 24g position, the lattice parameters of the skutterudite phase at higher tin content increase rapidly. Rietveld refinements of the x-ray patterns of $Ni_4Sb_9Sn_3$, $Ni_4Sb_{8.75}Sn_{3.25}$ and $Ni_4Sb_{8.5}Sn_{3.5}$ confirm the $CoAs_3$ structure (table 3), and R_F-values of <5% were obtained. However, x-ray profiles of alloys richer in Sn could not be treated properly in the $CoAs_3$ structure, yielding R_F-values above 8%. A significant improvement of the structure description was achieved by assuming a partial occupancy of the 2a position by additional Sn atoms. The choice of Sn atoms in the 2a site is consistent with the lattice expansion observed with increasing tin content. The refinement of the 2a site occupancy was started after the final refinement of all other parameters and an initial value of 0.5 was used as the temperature factor. A maximal level of occupancy of about 30% was obtained for the tin-rich sample, accompanied by large thermal displacement parameters (table 3). This result is comparable with the data of [4], reporting displacement parameters of 7.3 and 8.6 Å^2 for $Sn_{0.5}Co_4Sb_{12}$ and $SnCo_4Sb_{12}$, respectively. Confirmation for such large displacement parameters can be found from single-crystal data obtained for $Sn_yNi_4Sb_{12-x}Sn_x$ and those for the related skutterudite $Eu_{0.8}Ni_4Sb_{5.8}Sn_{6.2}$ (table 3). One can see reasonable isotropic displacement parameters obtained for Eu atoms in the 2a site. It is interesting to note that even at higher levels of occupancy of 80 and 60%, as obtained for the Eu-and Yb-containing compounds, the lattice parameters are close to those of tin-rich

Table 3a. Structural data (Rietveld refinements) for $Ni_4Sb_9Sn_3$ and $Sn_{0.31}Ni_4Sb_{6.4}Sn_{5.6}$, ($CoAs_3$–$LaFe_4P_{12}$ type, space group $Im\bar{3}$; No 204).

Parameter	$Ni_4Sb_9Sn_3$	$Sn_{0.31}Ni_4Sb_{6.4}Sn_{5.6}$	$Sn_{0.31}Ni_4Sb_{6.4}Sn_{5.6}$
Structure type	$CoAs_3$	$LaFe_4P_{12}$	$LaFe_4P_{12}$
Composition, (EMPA; at.%)	24.0Ni57.1Sb18.9Sn	23.5Ni39.9Sb36.5Sn	23.5Ni39.9Sb36.5Sn
a (nm)	0.910 85(1)	0.915 51(2)	0.915 75(2)
Data collection	Image plate	Image plate	Kappa CCD—single crystal
Radiation	Cu Kα	Cu Kα	Mo Kα
Reflections measured	81	84	7132 (332 unique)
Θ range	$8 \leqslant 2\Theta \leqslant 100$	$8 \leqslant 2\Theta \leqslant 100$	$2 \leqslant 2\Theta \leqslant 70$
Number of variables	23	24	11
$R_F = \sum |F_o - F_c|/\sum F_o$	0.038	0.048	0.049 ($319 F_o > 4\sigma$)
$R_I = \sum |I_o - I_c|/\sum I_o$	0.051	0.062	$\mu = 27.0$ mm^{-1}
$R_{wP} = [\sum w_i |y_{oi} - y_{ci}|^2/ \sum w_i |y_{oi}|^2]^{1/2}$	0.095	0.085	$R_{merge} = 0.056$
$R_P = \sum |y_{oi} - y_{ci}|/\sum |y_{oi}|$	0.070	0.062	—
$R_e = [(N - P + C)/\sum w_i y_{oi}^2)]^{1/2}$	0.038	0.027	—
$\chi^2 = (R_{wP}/R_e)^2$	6.13	9.7	GOF $= 1.27$
Atom parameters			
Sn1: in 2a (0, 0, 0)	—	Sn1	Sn1
B_{iso} (10^2 nm^2)	—	13.8(5)	$U_{iso} = 0.112(-)$
Occupancy	—	0.305(2)	0.30(3)
Ni: in 8c ($\frac{1}{4}, \frac{1}{4}, \frac{1}{4}$)	8Ni	8Ni	8Ni
B_{iso} (10^2 nm^2)	1.46(3)	1.41(4)	$U_{equ} = 0.0104(5)^a$
Occupancy	1	1	1
(Sb, Sn): in 24g (0, y, z)	18Sb + 6Sn	12.8Sb + 11.2Sn2	12.8Sb + 11.2Sn2
y	0.157 55(5)	0.160 07(6)	0.160 06(9)
z	0.335 26(5)	0.335 62(6)	0.337 25(10)
B_{iso} (10^2 nm^2)	1.84(1)	2.38(1)	$U_{equ} = 0.0162(4)^a$
Occupancy	1	1	1
Interatomic distances (nm); standard deviations generally <0.0005 nm			
Sn1–12Sb	0.3374	0.3404	0.3419
Ni–6Sb	0.2549	0.2555	0.2561
Ni–2Sn1	0.3944	0.3964	0.3965
Sb–2Ni	0.2549	0.2555	0.2561
Sb–1Sb	0.2870	0.2930	0.2931
Sb–1Sb	0.3001	0.3009	0.2981
Sb–1Sn1	0.3374	0.3404	0.3419

[a] Principal mean square atomic displacements (10^2 nm^2): Ni: $U_{11} = 0.0134(5)$; $U_{22} = 0.0089(4)$, $U_{33} = 0.0089(4)$; (Sb, Sn): $U_{11} = 0.0288(5)$, $U_{22} = 0.0109(4)$, $U_{33} = 0.0088(4)$; crystal structure data were standardized using the program TYPIX [46].

$Sn_yNi_4Sb_{12-x}Sn_x$, in which only 30% of the 2a positions are filled by Sn, which has a much smaller atomic radius in comparison with rare-earth elements. On the other hand, we can see that even in unfilled skutterudites (for example $CoSb_3$ which has an abnormally small lattice parameter), the distance between the 2a site and next-nearest atoms is already larger than the diameter of the Sn atom. With such a large hole, one can expect rather high displacement parameters for small atoms, such as Sn, rattling in this cage. In figure 3(b) one can see a smooth correlation of the 2a site occupancy by tin, as a function of the skutterudite lattice parameters. It should be noted that an increase of the tin content renders the skutterudite structure more regular: the sum of coordinates $y + z$ for atoms in 24g moves to the ideal value

Table 3b. Structural data (Rietveld refinements) for $Eu_{0.8}Ni_4Sb_{5.8}Sn_{6.2}$, $Yb_{0.6}Ni_4Sb_{6.7}Sn_{5.3}$ and $Ni_4As_{9.1}Ge_{2.9}$ ($CoAs_3$–$LaFe_4P_{12}$ type, space group $Im\bar{3}$; No 204).

Parameter	$Eu_{0.8}Ni_4Sb_{5.8}Sn_{6.2}$	$Yb_{0.6}Ni_4Sb_{6.7}Sn_{5.3}$	$Ni_4As_{9.1}Ge_{2.9}$
Structure type	$LaFe_4P_{12}$	$LaFe_4P_{12}$	$CoAs_3$
Composition (EMPA; at.%)	5.3Eu22.9Ni34.8Sb37.0Sn	4.7Yb23.3Ni40.5Sb31.5Sn	24.5Ni57.1As18.4Ge
a (nm)	0.915 88(2)	0.913 99(3)	0.828 73(3)
Data collection	Image plate	Image plate	Image plate
Radiation	Cu Kα	Cu Kα	Cu Kα
Reflections measured	84	84	63
Θ range	$8 \leqslant 2\Theta \leqslant 100$	$8 \leqslant 2\Theta \leqslant 100$	$8 \leqslant 2\Theta \leqslant 100$
Number of variables	24	24	23
$R_F = \sum |F_o - F_c| / \sum F_o$	0.032	0.042	0.050
$R_I = \sum |I_o - I_c| / \sum I_o$	0.035	0.051	0.078
$R_{wP} = [\sum w_i |y_{oi} - y_{ci}|^2 / \sum w_i |y_{oi}|^2]^{1/2}$	0.068	0.047	0.135
$R_P = \sum |y_{oi} - y_{ci}| / \sum |y_{0i}|$	0.049	0.055	0.096
$R_e = [(N - P + C) / \sum w_i y_{oi}^2)]^{1/2}$	0.036	0.023	0.036
$\chi^2 = (R_{wP}/R_e)^2$	3.7	9.8	14.0
Atom parameters			
E: in 2a (0, 0, 0)	Eu	Yb	—
B_{iso} (10^2 nm^2)	1.60(7)	1.8(1)	—
Occupancy	0.812(5)	0.58(4)	—
Ni: in 8c ($\frac{1}{4}, \frac{1}{4}, \frac{1}{4}$)	8Ni	8Ni	8Ni
B_{iso} (10^2 nm^2)	1.84(3)	1.60(6)	1.18(4)
Occupancy	1	1	1
X: in 24g (0, y, z)	11.6Sb + 12.4Sn	13.4Sb + 10.6Sn	18.2As + 5.8Ge
y	0.160 91(6)	0.1596(1)	0.150 31(7)
z	0.339 17(5)	0.3363(1)	0.344 60(7)
B_{iso} (10^2 nm^2)	2.00(1)	2.11(2)	1.30(2)
Occupancy	1	1	1
Interatomic distances (nm); standard deviations generally <0.0005 nm			
E–12X	0.3438	0.3402	0.3116
Ni–6X	0.2564	0.2555	0.2364
Ni–2E	0.3966	0.3958	0.3589
X–2Ni	0.2564	0.2555	0.2364
X–1X	0.2946	0.2992	0.2576
X–1X	0.2947	0.2917	0.2491
X–1E	0.3438	0.3402	0.3116

$\frac{1}{2}$ established by Oftedal [41]. It seems to appear for equiatomic Sb/Sn occupancy of the 24g site, which is not realized in the $Sn_yNi_4Sb_{12-x}Sn_x$ skutterudite, but it was obtained for the compound $Eu_{0.8}Ni_4Sb_{5.8}Sn_{6.2}$, in which $y + z$ is $\frac{1}{2}$ and, therefore, the two X–1X bonds have equal lengths (table 3).

A detailed analysis of the x-ray intensities of a single-crystal fragment of $Sn_{0.31}Ni_4Sb_{6.4}Sn_{5.6}$ confirmed the random distribution of Sb/Sn atoms in the 24g sites of space group $Im\bar{3}$ (see table 3). There is a significant electron density at the centre of the Sb/Sn icosahedron corresponding to a 30% occupancy of site 2a by Sn atoms, in agreement with x-ray powder data as well as with Mössbauer analysis (see below). At this level the atomic vibration of the atoms in the 2a site is about ten times that of the Sb/Sn framework atoms. There is, however, still a residual electron density of about six electrons located at a 16f position (0.051, 0.051, 0.051), which either can be interpreted as 'diffraction ripple' around the heavy (Sb/Sn)
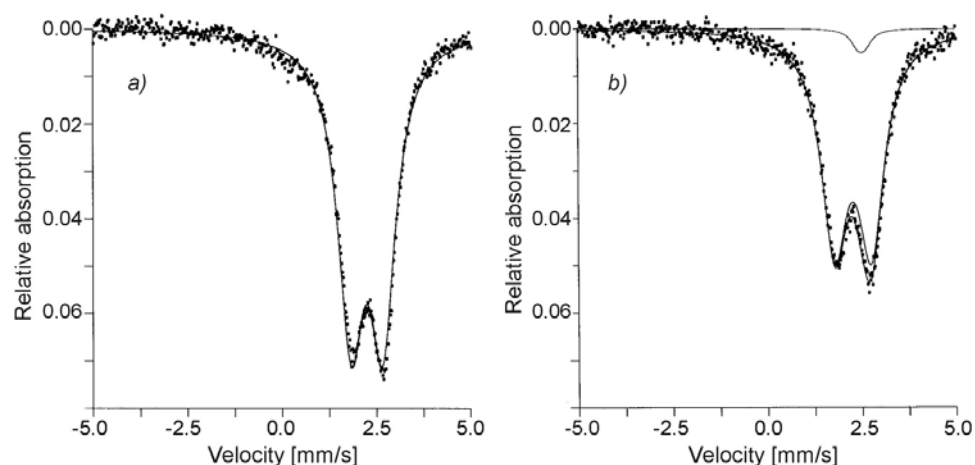
Figure 5. Mössbauer spectra of $Ni_4Sb_9Sn_3$ (a) and of $Sn_{0.21}Ni_4Sb_{7.1}Sn_{4.9}$ (b) at room temperature. The calculated total intensities and subspectra are represented by solid curves.

**Table 4.** Mössbauer parameters of $Ni_4Sb_9Sn_3$ and of $Sn_{0.21}Ni_4Sb_{7.1}Sn_{4.9}$ at room temperature. Isomer shift δ relative to SnO_2, halfwidth Γ, quadrupole splitting QS, area distribution A and goodness-of-fit parameter χ^2 as defined in the text.

Sample	Subspectra	δ (mm s^{-1})	Γ (mm s^{-1})	QS (mm s^{-1})	A (%)	χ^2
$Ni_4Sb_9Sn_3$	I	2.24(2)	0.8(4)	0.8(2)	100	0.57
$Sn_{0.21}Ni_4Sb_{7.1}Sn_{4.9}$	I	2.26(2)	0.8(3)	0.9(2)	96.5	0.39
	II	2.51(2)	0.4(1)	0.2(2)	3.5	

atoms (Fourier series termination error) or can be taken as a sign of a partially occupied atom position. A trial refinement placing Sn atoms in the 16f site (alternatively to Sn in 2a) yields an expected lowering of the R-value from 4.8 to 3.1% at an occupancy level of 9.3(6)% and a temperature motion of $U_{eq} = 0.069(5)$ (10^2 nm^2). It should be noted that the interatomic distances $d_{Sn-Sb} = 0.3419$ nm for Sn in 2a are far larger than the expected sum of radii, whilst $d_{Sn-Sb} = 0.283$ nm for Sn in 16f matches quite well the sum of the metal bonds. Still 'diffraction ripples' of about three electrons remain for a position (0.077, 0.063, 0).

The Mössbauer spectra obtained were fitted with a conventional refinement program [42]. In particular, the well-resolved patterns at room temperature (RT), as shown in figure 5, could easily be decomposed into one or two subspectra, that can be associated with each of the two crystallographic sites in question (24g or 24g + 2a). The corresponding parameters are summarized in table 4.

Even by visual inspection of figure 5, the difference between the spectra corresponding to the two samples is evident: whereas figure 5(a) ($Ni_4Sb_9Sn_3$) displays a quite well-resolved unique doublet, the asymmetry of the pattern in figure 5(b) ($Sn_{0.21}Ni_4Sb_{7.1}Sn_{4.9}$) suggests a second subspectrum under the high-velocity line. The χ^2-value drops considerably on introducing the second component; its isomer shift is different to that of the main doublet (attributed to the 24g site) and can be ascribed to the 2a position as predicted by the structure refinement. The calculated area (or partial tin content) of 3.5% on 2a relative to 24g is in good agreement with the relative site occupation as predicted by the crystallographic data (4.1%)
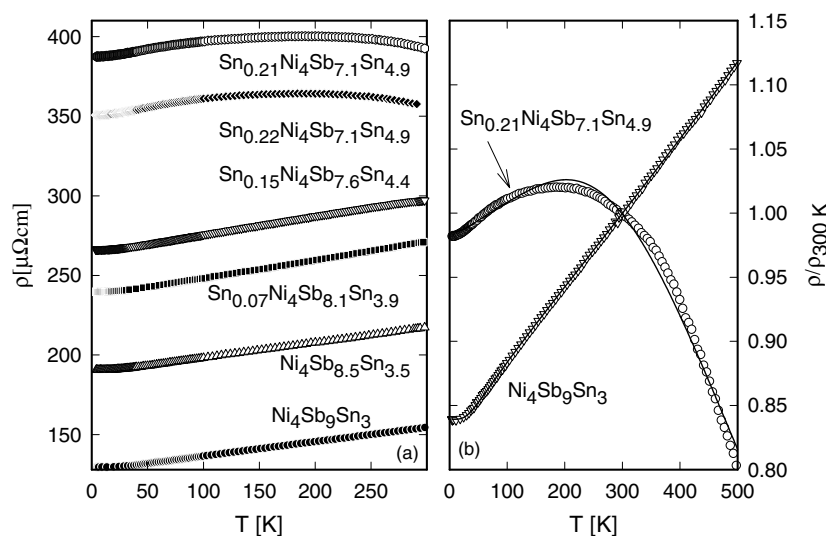
Figure 6. (a) Temperature-dependent resistivity $\rho(T)$ of $Sn_y Ni_4 Sb_{12-x} Sn_x$. (b) Normalized resistivity $\rho(T)/\rho(300\text{ K})$ of $Ni_4 Sb_9 Sn_3$ and $Sn_{0.21} Ni_4 Sb_{7.1} Sn_{4.9}$. The solid curves are least-squares fits according to equation (1) for $Ni_4 Sb_9 Sn_3$ and equation (2) for $Sn_{0.21} Ni_4 Sb_{7.1} Sn_{4.9}$.

taking an estimated absolute error of ∼1% (Mössbauer refinement) into account. Another hint of the validity of our site attribution is provided by the nearly vanishing quadrupole splitting (single curve, figure 5(b)), which corresponds to the comparably high isotropic temperature factor at 2a. On the other hand, the $Ni_4 Sb_9 Sn_3$ spectrum (figure 5(a)) requires no second subpattern—it can be refined with a sole doublet yielding an isomer shift and quadrupole splitting similar to the symmetrical part of the other sample and can be equally ascribed to the 24g site. Generally speaking, the results of the Mössbauer evaluations are in good agreement with the crystallographic findings.

3.3. Physical properties

The interesting peculiarity of the $Sn_y Ni_4 Sb_{12-x} Sn_x$ skutterudite is its existence over a wide homogeneity region and the occupancy of both the 2a and 24g sites by tin, prompting a detailed investigation of physical properties as a function of composition. A summary of the physical properties is given in figures 6–12.

3.3.1. Electrical resistivity. The temperature-dependent electrical resistivity $\rho(T)$ of $Sn_y Ni_4 Sb_{12-x} Sn_x$ is shown in figure 6(a). This series of compounds is characterized by relatively large values of the electrical resistivity, where the samples richest in Sn no longer exhibit metallic behaviour. The initial increase of the overall resistivity seems to be correlated with a decrease of the free carrier concentration when proceeding from $Ni_4 Sb_9 Sn_3$ to $Sn_{0.15} Ni_4 Sb_{7.6} Sn_{4.4}$. Although the method used to evaluate the number of carriers is simply based on crystal chemistry arguments, the evaluation of $\rho(T)$ upon substitution seems to adhere to the findings of this straightforward carrier counting method. The concentration-dependent change of carriers is additionally seen in the evolution of the Seebeck coefficient throughout the entire homogeneity range (see below). The temperature-dependent resistivity $\rho(T)$ of unfilled
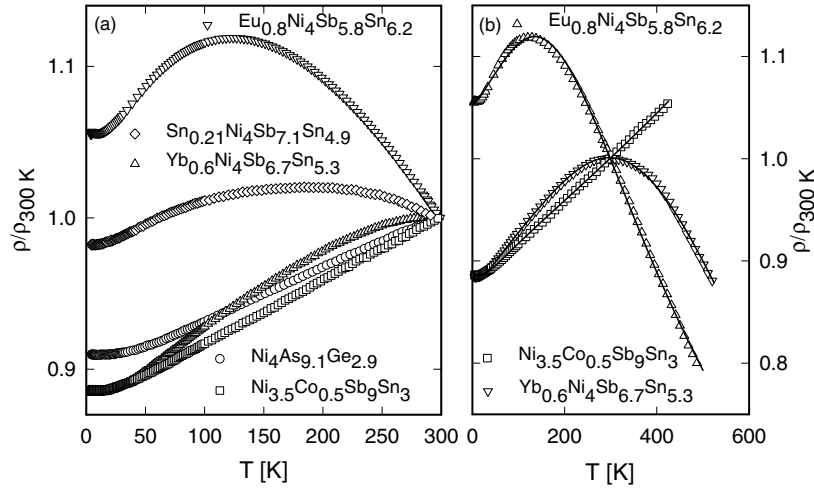
Figure 7. (a) Normalized resistivity $\rho/\rho_{300\,K}$ of $Sn_{0.21}Ni_4Sb_{7.1}Sn_{4.9}$, $Eu_{0.8}Ni_4Sb_{5.8}Sn_{6.2}$, $Yb_{0.6}Ni_4Sb_{6.7}Sn_{5.3}$, $Ni_4As_{9.1}Ge_{2.9}$ and $Ni_{3.5}Co_{0.5}Sb_9Sn_3$. (b) Normalized resistivity $\rho/\rho_{300\,K}$ of $Ni_{3.5}Co_{0.5}Sb_9Sn_3$, $Eu_{0.8}Ni_4Sb_{5.8}Sn_{6.2}$ and $Yb_{0.6}Ni_4Sb_{6.7}Sn_{5.3}$. The solid curves are least-squares fits according to equation (1) (for the former sample) and equation (2) (for both latter samples).

skutterudites, as shown in figure 6(a), was accounted for in terms of the Bloch Grüneisen formula

$$\rho(T) = \rho_0 + 4R\Theta_D \left(\frac{T}{\Theta_D}\right)^5 \int_0^{\Theta_D/T} \frac{x^5 \, dx}{(e^x - 1)(1 - e^{-x})} \tag{1}$$

with ρ_0 the residual resistivity, Θ_D the Debye temperature and R a temperature-independent electron–phonon interaction constant. Least-squares fits of equation (1) to the experimental data reveal Debye temperatures typical for soft intermetallic compounds ($\Theta_D \approx 165$–185 K). Replacing the large Sb, Sn atoms by elements with lower mass numbers, As, Ge, naturally introduces a higher degree of covalent bonding with significantly increased $\Theta_D \approx 260$ K. Besides an increase of ρ_0, the electron–phonon interaction constant R also concomitantly augments for $Ni_4As_{9.1}Ge_{2.9}$ (figure 7).

The temperature-dependent electrical resistivities of $Sn_{0.21}Ni_4Sb_{7.1}Sn_{4.9}$ (compare figure 6(b)), as well as $\rho(T)$ for $Eu_{0.8}Ni_4Sb_{5.8}Sn_{6.2}$ and $Yb_{0.6}Ni_4Sb_{6.7}Sn_{5.3}$ (figure 7(b)), exhibit two different regimes: a metallic-like regime at low temperatures and a semiconducting-like regime at elevated temperatures, at least up to 500 K. The latter, however, is not characterized by a simple activation-type conduction mechanism. In order to account for this rather complicated temperature dependence, we consider a model density of states, where a narrow gap lies slightly above the Fermi energy. This implies that a number of unoccupied states above $E = E_F$ are available at $T = 0$. As a consequence, metallic conductivity is possible at low temperatures, until the limited number of states slightly above E_F become involved in the transport process. For further transport processes of the charge carriers, electrons have to be excited across the energy gap with width E_{gap}. The total number of carriers available in this process, $n(T)$, i.e., electrons and holes, is strongly dependent on E_{gap} as well as on the absolute temperature, and follows from general statistical laws. On the basis of these assumptions, $\rho(T)$ can be calculated from

$$\rho(T) = [\rho_0 + \rho_{ph}]/n(T) \tag{2}$$

where ρ_0 is the residual resistivity and ρ_{ph} describes the scattering of electrons on phonons, accounted for in terms of the Bloch Grüneisen law (equation 1). Least-squares fits

according to equation (2) were performed for $Sn_{0.21}Ni_4Sb_{7.1}Sn_{4.9}$, $Eu_{0.8}Ni_4Sb_{5.8}Sn_{6.2}$ and $Yb_{0.6}Ni_4Sb_{6.7}Sn_{5.3}$, revealing gap widths of 1900, 900 and 2400 K (162, 77 and 205 meV) respectively, tracing nicely the composition-dependent shift of the resistivity maximum (compare figures 6(a) and 7(a)).

Attempts were also made to describe $\rho(T)$ in terms of Mott's variable-range hopping conductivity mechanism [43]. However, neither the $T^{1/4}$-term nor a $T^{1/2}$-term is sufficient to explain the experimental findings.

3.3.2. Raman spectroscopy, specific heat and magnetic properties. According to space group $Im\bar{3}$ (T_h^5), Sb and Sn occupying the 24g site contribute with their vibrations to $2A_g + A_u + 2E_g + E_u + 4F_g + 5F_u$ irreducible representations, the Ni on 8c to $A_u + E_u + 3F_u$, the Sn on the filling position 2a to F_u and the possible position 16f found in x-ray analysis will contribute to $A_g + A_u + E_g + E_u$. Only the gerade representations will cause Raman scattering.

The two strongest modes at 115 and 150 cm^{-1} are assigned to the two intrinsic A_g modes arising from the 24g site of the Sb, Sn atoms and are comparable with the strongest modes in other skutterudites such as $CoSb_3$ [44, 45]. However, the frequencies are much lower as compared to other skutterudites, indicating lower stability and lower binding forces of the Ni compound. We were able to identify all the $2A_g$, $2E_g$ and $4F_g$ modes arising from the 24g site, although, as expected, the selection rules are not as strict as perfect symmetry requires. Additional observed modes are either some of the usual non-Raman-active modes which become allowed by symmetry breaking or ones that belong to the already known disorder modes predominantly observed in laser-damaged samples. Since x-ray scattering has not revealed impurity phases in the crystals, the disorder modes have to be interpreted as indications of modified atomic positions. One can assume that at least one of the disorder modes belongs to the filling site at 16f. The x-ray investigations are not in contradiction with a small occupation (∼9%) of the 16f site with a displacement of ∼0.07 Å^2 at room temperature. At such small occupation numbers we do not expect a multiplicity of 16 and the Sn atom should behave like a defect mode. Thus only one to maximally three modes can be expected to arise from a partial 16f occupation with a frequency around 80 cm^{-1}. The mode at 76 cm^{-1} probably satisfies these conditions. The dependence on localization on the sample indicates that the occupation of the 16f site varies over the sample volume. The strong increase in Raman intensity with higher laser densities leads to a prediction of a higher occupation at elevated temperatures. In principle, there should be the same conditions for the 2a site but with much higher occupation (∼30%). Lifted symmetry selection rules are also expected, providing Raman activity and a defect-like behaviour. Because of the strongly enhanced displacement values of the 2a site, much lower Raman frequencies can be assumed below the observed range of our measurements.

Figure 8 compares the heat capacity C_p of $Sn_{0.21}Ni_4Sb_{7.1}Sn_{4.9}$, $Eu_{0.8}Ni_4Sb_{5.8}Sn_{6.2}$ and $Yb_{0.6}Ni_4Sb_{6.7}Sn_{5.3}$, as C_p/T versus T. Since magnetic contributions are absent in $Sn_{0.21}Ni_4Sb_{7.1}Sn_{4.9}$, $Yb_{0.6}Ni_4Sb_{6.7}Sn_{5.3}$, the specific heat is simply a sum of the electronic part, $C_{el}(T)$, and the lattice part, $C_{ph}(T)$. Interpreting the data by a standard procedure yields the Sommerfeld value $\gamma = 12$ mJ mol^{-1} K^{-2} as well as $\Theta_D = 179$ K. In order to understand the lattice dynamics of such systems, the specific heat is analysed in a first attempt considering a Debye spectrum together with two Einstein modes, and additionally, in order to account for the behaviour of the weakly bound filler element Sn, considering a single Einstein contribution, i.e.,

$$C_{ph}(T) = 4\frac{9R}{\omega_D^3}\int_0^{\omega_D}\frac{\omega^2(\frac{\omega}{2T})^2}{\sinh^2(\frac{\omega}{2T})}\,d\omega + \sum_{i=1,2,3}c_i R\frac{(\frac{\omega_{Ei}}{2T})^2}{\sinh^2(\frac{\omega_{Ei}}{2T})}. \tag{3}$$
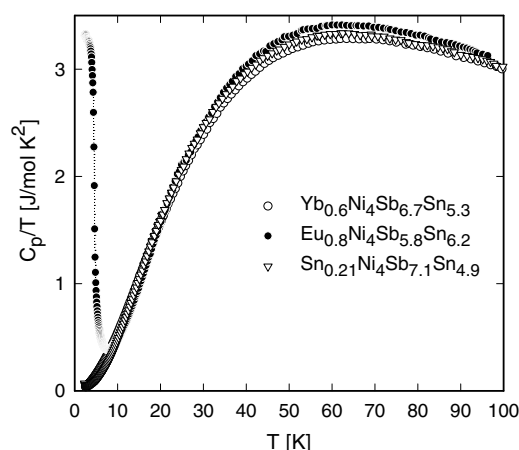
Figure 8. The temperature-dependent specific heat C_P of $Sn_{0.21}Ni_4Sb_{7.1}Sn_{4.9}$, $Eu_{0.8}Ni_4Sb_{5.8}Sn_{6.2}$ and $Yb_{0.6}Ni_4Sb_{6.7}Sn_{5.3}$ plotted as C_p/T versus T.

Using $c_1 = 27$ and $c_2 = 9$, equation (3) already yields a reasonable parametrization of the whole temperature dependence from 2 to 120 K. Thereby, the three acoustic and nine optical branches of the phonon dispersion of the $(Ni_4Sb_9Sn_3)$ framework are represented by (12 times) one Debye and two Einstein functions $(27f_{E1} + 9f_{E2})$. To account for filled skutterudites, we simply added one further Einstein function to describe the increased number of phonon modes due to additional Sn atoms in the icosahedral voids, with $c_3 = 3y$, where y is the degree of void filling. The parameters obtained by least-squares fits of the experimental data reveal $\omega_D = 132$ K, $\omega_{E1} = 258$ K, $\omega_{E2} = 134$ K and $\omega_{E3} = 41$ K for $y = 0.22$. A similar set of frequencies were obtained for $Yb_{0.6}Ni_4Sb_{6.7}Sn_{5.3}$. One should note that the Einstein frequency associated with the filler element is rather low: $\omega_{E3} = 41$ K for the Sn-filled compound and $\omega_{E3} = 56$ K for the Yb-filled analogue. In comparison with binary, unfilled compounds such as $CoSb_3$ or $RhSb_3$ [33], the filled skutterudites do not just exhibit an additional weak Einstein (rattling) mode; rather, the whole lattice softens if electropositive elements fill the large cages of this structure.

At low temperatures, $C_P(T)$ of $Eu_{0.8}Ni_4Sb_{5.8}Sn_{6.2}$ exhibits a lambda-like anomaly due to the onset of magnetic order below about 6 K. The magnetic entropy S_{mag}, associated with this transition and evaluated up to 7 K, is revealed as $S_{mag} \approx R \ln 8$, resembling clearly that of a magnetic Eu^{2+} state with $J = 7/2$. The absence of orbital contributions in this particular case is concomitant with the absence of crystal field effects; hence the paramagnetic temperature range in the specific heat is primarily represented by the phonon part. A comparison of the specific heat data as shown in figure 8 underlines this conclusion.

Taking into account the 14 Raman-active frequencies (out of a total of 48 possible frequencies for the unfilled framework of the structure—36 Einstein frequencies plus 12 Debye modes), ranging within the limits of experiment from $\nu = 59$ cm^{-1} (85 K) to 205 cm^{-1} (295 K), an acceptable fit can only be achieved when at least one low-lying frequency around 40–50 K is invoked. The latter is well below the experimental limit of the Raman spectrometer employed. Furthermore, the least-squares fits certainly did not yield frequencies higher than 300 K, in agreement with the low melting point of the material investigated as well as with the rather low Debye temperature.

Isothermal magnetization measurements and the temperature-dependent susceptibility for $Eu_{0.8}Ni_4Sb_{5.8}Sn_{6.2}$ are shown in figure 9. The magnetization measured at 4 K shows a rapid
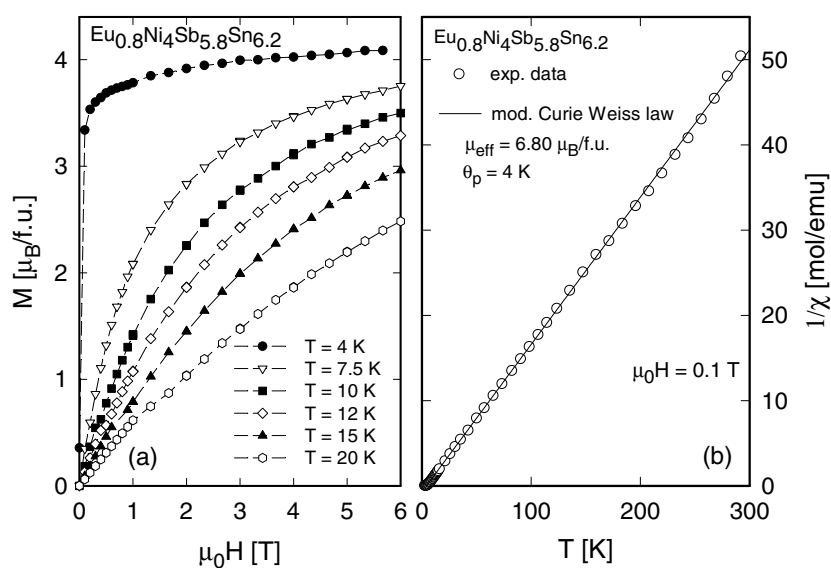
Figure 9. (a) The isothermal magnetization of $Eu_{0.8}Ni_4Sb_{5.8}Sn_{6.2}$. (b) The temperature-dependent magnetic susceptibility χ of $Eu_{0.8}Ni_4Sb_{5.8}Sn_{6.2}$ plotted as $1/\chi$ versus T. The solid line is a least-squares fit according to a modified Curie–Weiss law.

saturation, revealing at 6 T a saturation moment of 4.1 μ_B, which is close to the theoretically expected value of 0.8 gJ = 5.6 μ_B. This deviation possibly gives a hint of a slightly canted or ferrimagnetic spin arrangement associated with the Eu ions. Evaluation of the susceptibility data in terms of a modified Curie–Weiss law yields $\mu_{eff} = 6.80\,\mu_B$ which compares well with the expected value for Eu^{2+} and a partial site filling of 80% ($\mu_{eff} = 7.09\,\mu_B$). These magnetic data evidence a predominant divalent ground state for Eu and corroborate the magnetic entropy analysis.

Magnetization measurements performed for $Yb_{0.6}Ni_4Sb_{6.7}Sn_{5.3}$ at 2 K yielded an extremely small magnetization of 0.03 μ_B at 6 T, consistent with essentially non-magnetic, divalent Yb.

A proof of the divalent character of Eu in $Eu_{0.8}Ni_4Sb_{5.8}Sn_{6.2}$ is obvious from the L_{III} absorption edge measurements performed at $T = 300$ and 10 K as shown in figure 10. Applying a standard deconvolution technique [30], as used in previous studies of Eu skutterudites, reveals a valence of roughly 2, almost independent of temperature. These data are in agreement with the appearance of magnetic order as also observed in $Eu_{0.83}Fe_4Sb_{12}$ and $Eu_y(Fe, Co)_4Sb_{12}$. There, long-range magnetic order occurs in a special type of mixed-valence state composed of Eu atoms in two different static electronic configurations [30].

3.3.3. Thermal conductivity. The temperature-dependent thermal conductivity $\lambda(T)$ of the Sn-based samples was measured for $Ni_4Sn_9Sn_3$ and for filled $Sn_{0.21}Ni_4Sb_{7.1}Sn_{4.9}$ and is displayed in figure 11(a). The overall thermal conductivity $\lambda(T)$ is characterized by a smooth increase with growing temperature; the stronger rise above about 220 K most probably originates from radiation losses according to the Stefan–Boltzmann law. A comparison of the two measurements clearly signals an overall and significant reduction of $\lambda(T)$ in the filled case. This, in fact, supports the scenario that the rattling mode, associated with the filler element, interacts intensely with the heat-carrying phonons, and as a consequence of the enhanced scattering processes the thermal conductivity is reduced.
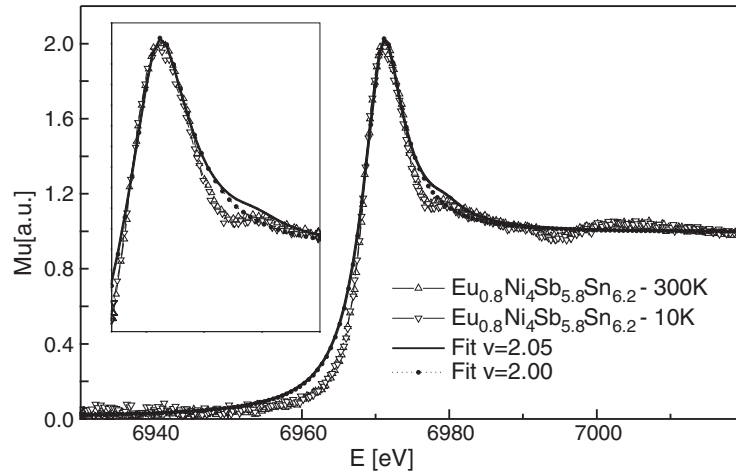
Figure 10. The energy-dependent L_{III} absorption edge of $Eu_{0.8}Ni_4Sb_{5.8}Sn_{6.2}$ at $T = 300$ and 10 K. The curves show the results of fits to the data with the valence $v = 2$ and 2.05.
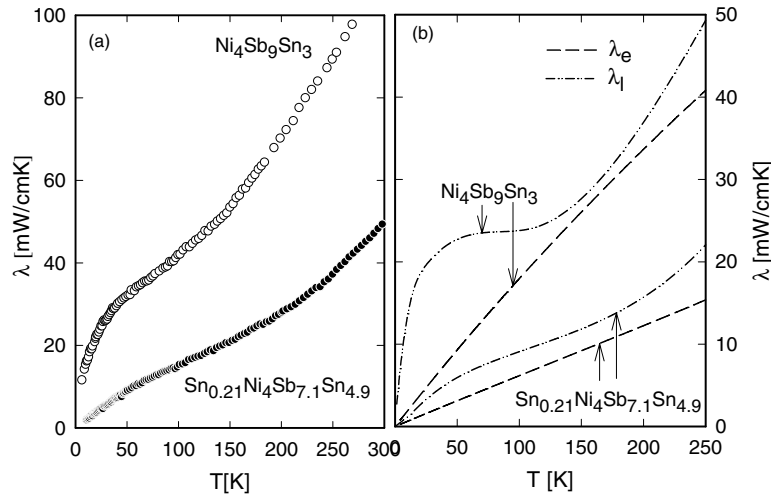
Figure 11. (a) The temperature-dependent thermal conductivity λ of $Sn_yNi_4Sb_{12-x}Sn_x$. (b) The electronic part (λ_e) and the lattice part (λ_l) of the total thermal conductivity λ of $Sn_yNi_4Sb_{12-x}Sn_x$.

The total thermal conductivity λ is usually given by $\lambda = \lambda_e + \lambda_l$ where λ_e represents the electronic part and λ_l the lattice contribution. Both individual contributions to λ are limited by a number of scattering processes, which are responsible for a finite thermal resistivity. In the case of simple metals, the Wiedemann–Franz law is expected to be valid, revealing $\lambda_e = L_0 T/\rho$. $L_0 = 2.45 \times 10^{-8}$ W Ω K^{-2} is the Lorenz number (derived within the free electron model) and ρ is the electrical resistivity of the sample. Once λ_e is derived, the lattice part λ_l can be calculated (see figure 11(b)). While λ_e is reduced from $Ni_4Sb_9Sn_3$ to $Sn_{0.21}Ni_4Sb_{7.1}Sn_{4.9}$ according to the increase of the electrical resistivity, owing to a reduced carrier number, the observed decrease of λ_l is assigned to scattering of the phonons on the soft modes of the filler element.
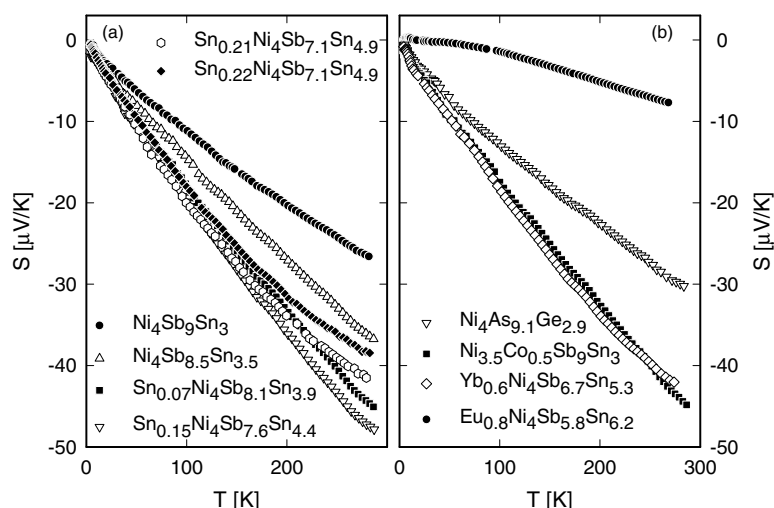
Figure 12. (a) The temperature-dependent thermopower S of $Sn_y Ni_4 Sb_{12-x} Sn_x$. (b) $S(T)$ of $Ni_4 As_{9.1} Ge_{2.9}$, $Ni_{3.5} Co_{0.5} Sb_9 Sn_3$, $Eu_{0.8} Ni_4 Sb_{5.8} Sn_{6.2}$ and $Yb_{0.6} Ni_4 Sb_{6.7} Sn_{5.3}$.

3.3.4. Seebeck effect. The Seebeck coefficient, shown in figure 12(a) for the series $Sn_y Ni_4 Sb_{12-x} Sn_x$, exhibits negative values throughout the temperature range covered, attaining about -50 μV K^{-1} near room temperature. The fact that $S(T)$ is negative can be associated with transport, dominated by electrons as charge carriers. The argumentation in the following is based on the findings in the literature, claiming $CoSb_3$ to be a semiconducting diamagnetic compound. Electron–hole balance can be achieved via chemical substitution in the transition metal and/or p-metal sublattices. For example, $Ni_4 Sb_9 Sn_3$ is assumed to be characterized by one electron as charge carrier (Ni electrons are partially compensated by the holes arising from the exchange of 3Sb with 3Sn atoms). Consequently, the corresponding thermopower is found to be negative. With increasing Sb/Sn substitution, the number of electrons is reduced. Since, in general, the absolute value of the Seebeck coefficient depends on the number of charge carriers, enlarged $S(T)$ values will be expected (see for instance $Ni_4 Sb_{8.5} Sn_{3.5}$; figure 12(a)). When the Sb/Sn substitution reaches the ratio Sb:Sn = 2, (at this point the Sb/Sn substitution reaches electroneutrality), additional Sn atoms tend to occupy the icosahedral voids of the structure, thereby providing supplementary electrons as charge carriers. The obviously small content of carriers further augments the Seebeck coefficient (see for instance $Sn_{0.07} Ni_4 Sb_{8.1} Sn_{3.9}$, figure 12(a)). Slightly different stoichiometries may optimize the number of charge carriers in order to maximize the Seebeck coefficient (see for instance $Sn_{0.15} Ni_4 Sb_{7.6} Sn_{4.4}$, figure 12(a)). Following this argumentation, it is conceivable that the Seebeck effect of $Ni_4 As_{9.1} Ge_{2.9}$ stays of the same order of magnitude as isotypic and homologous $Ni_4 Sb_9 Sn_3$ (figure 12(b)). Similarly, Ni/Co exchange also reduces the electron count, enhancing $S(T)$ (see $Ni_{3.5} Co_{0.5} Sb_9 Sn_3$; figure 12(b)). On insertion of large electropositive rare-earth elements into the icosahedral voids of the structure, such as in $Yb_{0.6} Ni_4 Sb_{6.7} Sn_{5.3}$ or $Eu_{0.8} Ni_4 Sb_{5.8} Sn_{6.2}$, we observe large or small Seebeck effects depending on the particular stage of electron/hole compensation (see figure 12(b)).

The figure of merit ZT ($ZT = TS^2/\rho\lambda$) for the filled and unfilled skutterudites $Ni_4 Sb_9 Sn_3$ and $Sn_{0.21} Ni_4 Sb_{7.1} Sn_{4.9}$ at room temperature approaches values of 0.014 and 0.03, respectively.

4. Summary

Novel skutterudites, $Sn_y Ni_4 Sb_{12-x} Sn_x$, as well as $Eu_{0.8} Ni_4 Sb_{5.8} Sn_{6.2}$, $Yb_{0.6} Ni_4 Sb_{6.7} Sn_{5.3}$ and $Ni_4 As_{9.1} Ge_{2.9}$, have been characterized with respect to formation and crystal structure. They all belong to a new series of skutterudites in which the 8c position of the structure is fully occupied by Ni. A variety of physical quantities were determined from L_{III} XAS, ^{119}Sn Mössbauer and Raman spectroscopy, magnetic and specific heat studies, as well as from measurements of transport coefficients (electrical resistivity, thermal conductivity and thermopower) as a function of composition, temperature and magnetic field. The investigation of phase equilibria in the Ni–Sb–Sn ternary system at 250 and 350 °C revealed a wide range of homogeneity of $Sn_y Ni_4 Sb_{12-x} Sn_x$, i.e., at 250 °C, $2.4 \leqslant x \leqslant 5.6$, $0 \leqslant y \leqslant 0.31$; at 350 °C, $2.7 \leqslant x \leqslant 5.0$, $0 \leqslant y \leqslant 0.27$. Sn atoms in $Sn_y Ni_4 Sb_{12-x} Sn_x$ occupy two crystallographically inequivalent sites:

(a) Sn and Sb atoms in random distribution share the 24g site; and
(b) a small fraction of Sn atoms occupy the 2a (0, 0, 0) position with large thermal motion parameters.

Within the homogeneity range, transport is primarily governed by the number of charge carriers, revealing a crossover from a metallic state in $Ni_4 Sb_9 Sn_3$ to a semiconducting behaviour in $Sn_{0.22} Ni_4 Sb_{7.1} Sn_{4.9}$. A model density of states with the Fermi energy slightly below a narrow energy gap perfectly aligns with the theoretical description of the temperature-dependent electrical conductivity. Inserting 4f elements (Eu, Yb) into the 2a sites introduces electron carriers compensating the hole-type conductivity of the framework. While the former causes the occurrence of long-range magnetic order, the latter triggers intermediate-valence behaviour.

Acknowledgments

References

[1] Hornbostel M D, Sellinschegg K and Johnson D C 1997 *Thermoelectric Materials—New Directions and Approaches (Mater. Res. Soc. Symp. Proc. Ser.)* vol 478 (Pittsburgh, PA: Materials Research Society) p 211
[2] Hornbostel M D, Hyer E J, Thiel J and Johnson D C 1997 *J. Am. Chem. Soc.* **119** 2665
[3] Takizawa H, Miura K, Ito M, Suzuki T and Endo T 1999 *J. Alloys Compounds* **282** 79
[4] Nolas G S, Takizawa H, Endo T, Sellinschegg H and Johnson D C 2000 *Appl. Phys. Lett.* **77** 52
[5] Takizawa H, Ito M, Uheda K and Endo T 2000 *J. Ceram. Soc. Japan* **108** 530
[6] Takizawa H, Okazaki K, Uheda K and Endo T 2001 *MRS Fall Meeting (Boston, MA, Nov. 2001)* (abstracts) p123
    Takizawa H, Okazaki K, Uheda K and Endo T 2002 *MRS Fall Meeting (Boston, MA, Nov. 2001) (Mater. Res. Soc. Symp. Proc. Ser. vol 691)* at press
[7] Liu H, Hu X, Wang J, Zhang C, Zhao S, Jiang H, Gu M and Zhang L 2001 *J. Cryst. Growth* **234** 679
[8] Koyanagi T, Tsubouchi T, Ohtani M, Kishimoto K, Anno H and Matsubara K 1996 *Proc. ICT '96: 15th Int. Conf. on Thermoelectrics* (New York: IEEE) p 107
[9] Nagamoto Y, Tanaka K and Koyanagi T 1997 *Proc. ICT '97: 16th Int. Conf. on Thermoelectrics* (New York: IEEE) p 330

[10] Nolas G S, Cohn J L and Slack G A 1998 *Phys. Rev.* B **58** 164
[11] Dilley N R, Bauer E D, Maple M B and Sales B C 2000 *J. Appl. Phys.* **88** 1948
[12] Sales B C, Chakoumakos B C and Madrus D 2000 *Phys. Rev.* B **61** 2475
[13] Sellinschegg H, Stuckmeyer S L, Hornbostel M D and Johnson D C 1998 *Chem. Mater.* **10** 1096
[14] Llunell M, Alemany P, Alvarez S, Zhukov V P and Vernes A 1996 *Phys. Rev.* B **53** 10 605
[15] Jeitschko W, Foecker A J, Paschke D, Dewalsky M V, Evers Ch B H, Kunnen B, Lang A, Kotzyba G, Rodewald U Ch and Moller M H 2000 *Z. Anorg. Allg. Chem.* **626** 1112
[16] Massalski T B (ed) 1990 *Binary Alloy Phase Diagrams* 2nd edn (Materials Park, OH: ASM International)
[17] Villars P and Calvert L D (ed) 1991 *Pearson's Handbook of Crystallographic Data for Intermetallic Phases* 2nd edn (Materials Park, OH: ASM International)
[18] Kjekshus A, Nicholson D G and Rakke T 1973 *Acta Chem. Scand.* **27** 1315
[19] Chapon L, Ravot D and Tedenac J C 1998 *C. R. Acad. Sci., Paris* **1** 761
[20] Chapon L, Ravot D and Tedenac J C 1999 *J. Alloys Compounds* **282** 58
[21] Chapon L, Ravot D and Tedenac J C 2000 *J. Alloys Compounds* **299** 68
[22] Grytsiv A *et al* 2002 to be submitted
[23] Grytsiv A, Rogl P, Berger S, Paul Ch, Bauer E, Godart C, Saccone A, Ferro R and Kaczorowski D 2001 *MRS Fall Meeting (Boston, MA, Nov. 2001)* (abstracts) p 132
    Grytsiv A, Rogl P, Berger S, Paul Ch, Bauer E, Godart C, Saccone A, Ferro R and Kaczorowski D 2002 *MRS Fall Meeting (Boston, MA, Nov. 2001) (Mater. Res. Soc. Symp. Proc. Ser. vol 691)* at press
[24] Gladyshevsky E I and Cherkashin E E 1955 *Nauchn. Zap. L'vov. Gos. Univ. (Ser. Khim.)* **34** 51
[25] Burkhardt W and Schubert K 1959 *Z. Metallk.* **50** 442
[26] Panteleimonov L A and Nesterova O P 1964 *Zh. Neorg. Khim.* (Engl. transl. *Russ. J. Inorg. Chem.* **9** 124)
[27] Dokuzoguz H K, Bowen L H and Stadelmaier H H 1970 *J. Phys. Chem. Solids* **31** 1565
[28] Heinrich S, Rexer H U and Shubert K 1978 *J. Less-Common Met.* **60** 65
[29] Rodriguez-Carvajal J 1990 *Satellite Mtg on Powder Diffraction of the 15th Congr. of the International Union of Crystallography (Toulouse, France)* (abstracts) p 127
[30] Grytsiv A *et al* 2001 *Phys. Rev.* B submitted
[31] *Nonius Kappa CCD Program Package COLLECT, DENZO, SCALEPACK, SORTAV* 1998 (Nonius Delft, The Netherlands)
[32] Sheldrick G M 1997 *SHELX-97, Program for Crystal Structure Refinement* University of Göttingen, Germany; Windows version by McArdle (National University of Ireland, Galway)
[33] Bauer E, Galatanu A, Michor H, Hilscher G, Rogl P, Boulet P and Noel H 2000 *Eur. Phys. J.* B **14** 483
[34] Barb D 1980 *Grundlagen und Anwendungen der Mössbauerspektroskopie* (Berlin: Akademie) pp 44–49
[35] Knoll P, Singer R and Kiefer W 1990 *Appl. Spectrosc.* **44** 776
[36] Predel B and Schwermann W 1971 *J. Instrum. Methods.* **99** 169
[37] Jönsson B and Agren J 1986 *Meas. Sci. Technol.* **2** 913
[38] Allen W P and Perepezko J H 1990 *Scr. Metall. Mater.* **24** 2215
[39] Ohtani H, Okuda K and Ishida K 1995 *J. Phase Equilib.* **16** 416
[40] Vassiliev V, Feutelais Y, Sghaier M and Legendre B 2001 *J. Alloys Compounds* **314** 198
[41] Oftedal I 1928 *Z. Kristallogr.* A **66** 517
[42] Lottermoser W, Kaliba P, Forcher K and Amthauer G 1994 *MOESALZ: a Program for Mössbauer Data Refinement* (University of Salzburg)
[43] Mott N F 1970 *Phil. Mag.* **22** 7
[44] Nolas G S and Kendziora C A 1999 *Phys. Rev.* B **59** 6189
[45] Li L X, Liu H, Wang J Y, Hu X B, Zhao S R, Jiang H D, Huang Q J, Wang H H and Li Z F 2001 *Chem. Phys. Lett.* **347** 373
[46] Parthe E, Gelato L, Chabot B, Penzo M, Cenzual K and Gladyshevskii R 1994 *TYPIX Standardized Data and Crystal Chemical Characterization of Inorganic Structure Types* (Berlin: Springer)